Review of Scientific Instruments

V-ONSET (Vertical Octagonal Noncorrosive Stirred Energetic Turbulence): A vertical water tunnel with a large energy dissipation rate to study bubble/droplet deformation and breakup in strong turbulence

Cite as: Rev. Sci. Instrum. **90**, 085105 (2019); https://doi.org/10.1063/1.5093688
Submitted: 23 February 2019 . Accepted: 09 July 2019 . Published Online: 13 August 2019

Ashik Ullah Mohammad Masuk, Ashwanth Salibindla, Shiyong Tan, and Rui Ni

Rev. Sci. Instrum. **90**, 085105 (2019); https://doi.org/10.1063/1.5093688 **90**, 085105

Review of Scientific Instruments | ARTICLE | scitation.org/journal/rsi

V-ONSET (Vertical Octagonal Noncorrosive Stirred Energetic Turbulence): A vertical water tunnel with a large energy dissipation rate to study bubble/droplet deformation and breakup in strong turbulence

Cite as: Rev. Sci. Instrum. 90, 085105 (2019); doi: 10.1063/1.5093688
Submitted: 23 February 2019 • Accepted: 9 July 2019 •
Published Online: 13 August 2019

Ashik Ullah Mohammad Masuk, Ashwanth Salibindla, Shiyong Tan, and Rui Ni[a)]

AFFILIATIONS

Department of Mechanical Engineering, Johns Hopkins University, Baltimore, Maryland 21218, USA

[a)] **Electronic mail:** rui.ni@jhu.edu

ABSTRACT

A vertical water tunnel facility has been constructed to study the dynamics of turbulent multiphase flow. The new system features several unique designs that allow us to study bubble deformation and breakup in strong turbulence: (i) The mean flow can be adjusted to balance the rising velocity of buoyant bubbles/droplets so that they can stay in the view area for an extended period of time. (ii) Turbulence is generated and controlled using a 3D-printed jet array that can fire 88 random high-speed momentum jets with the individual jet velocity of up to 12 m/s. This component allows us to attain turbulence with a high energy dissipation rate (≥ 0.1 m^2/s^3), which is orders-of-magnitude higher than most of the existing turbulent multiphase flow facilities. (iii) Turbulence generated in the test section is nearly homogeneous and isotropic, and the turbulent fluctuations are also decoupled from the mean flow. The resulting turbulence intensity can be varied between 20% and 80% with the speed of the mean flow at around 0.2 m/s. (iv) This system has an octagonal test section that allows six cameras to image and reconstruct the 3D shape of deforming bubbles/droplets in turbulence. The same set of cameras was also used for tracking tracers in the surrounding turbulent flow. Both the reconstruction and particle tracking were completed using our in-house codes that were parallelized to run on high-performance computing clusters efficiently.

I. INTRODUCTION

From dust storms to breaking waves, flows in nature are often turbulent and concentrated with elements in a different phase, such as gas bubbles, oil droplets, or solid aggregates. In these types of flows that are often associated with large length scales and abundant kinetic energy, both the Reynolds number (*Re*) and the energy dissipation rate $\varepsilon = 2\nu\langle S_{ij}S_{ij}\rangle$ are large (ν is the kinematic viscosity and S_{ij} represents the rate-of-strain tensor). Numerous facilities have been built to target high Reynolds numbers. These facilities include classical wind tunnels, water tunnels, large-scale pipe flow facility,[1] coaxial counter-rotating disks system,[2] and Taylor-Couette setups,[3–5] as well as other systems that use more exotic working fluid, such as the variable pressure facilities,[6,7] liquid metal experiments,[8] and cryogenic liquid studies.[9] In comparison with this decades-long effort, the effect of the high energy dissipation rate has not been paid much attention, even though it is more important than *Re* in multiphase flow. In multiphase flow, the dispersed phase is typically very small in size; for these dispersed elements, the large-scale flow is less important compared with the small-scale local flow around them, which is controlled by ε. Although ε is not a dimensionless number, it can be converted to the particle Stokes number *St* or the Weber number *We*.

We measures the ratio between the turbulent stress acting on bubbles and the restoring stress σ/l_b by the surface tension. The turbulent stress on bubbles of finite size l_b ($l_b \gg \eta$) can be related to the energy dissipation rate following the second-order structure function as $\tau = C_2\rho(\varepsilon l_b)^{2/3}$.[10,11] C_2, ρ, and η are the Kolmogorov constant, density of the carrier phase, and the Kolmogorov length scale, respectively. As a result, $We = C_2\rho(\varepsilon l_b)^{2/3} l_b/\sigma$. For $We \ll 1$, the surface tension is dominant and bubbles stay spherical. For $We \gg 1$, bubbles can be deformed and even broken by turbulence. As one can see from the definition of We, a large We requires a large ε, which motivates us to build a turbulence facility targeting large ε.

In addition to We, bubble deformation can also be affected by its buoyancy, which is determined by the Eötvös number, i.e., $Eo = \Delta\rho g l_b^2/\sigma$. To make sure that the turbulence-induced deformation outweighs the buoyancy-induced one, one would need to have $We \geq Eo \geq 1$, which provides two equations for two unknowns, ε and l_b, assuming other parameters related to the fluid physical properties are constant. Based on the calculation, the minimum requirement is that the mean energy dissipation rate $\varepsilon \geq 0.57$ m^2/s^3 for bubbles with sizes in a small range near 2.7 mm. For ε much smaller than $O(0.1)$ m^2/s^3, bubbles of all sizes will be dominated either by the surface tension (small sizes) or the buoyancy (large sizes), never by turbulence—even with the help of turbulence intermittency. If one can afford a larger mean energy dissipation rate, the size range of bubbles that is controlled by turbulence will become wider. Note that this calculation is to provide an order-of-magnitude estimation rather than a specific number, as the critical Weber number for bubble deformation is of order unity rather than the value of one. So the goal of the designed facility is to reach $\varepsilon \approx O(0.1)$ m^2/s^3.

Using the second-order structure function to estimate turbulent stress on bubbles is a standard practice in the chemical engineering community to study steady-state emulsion droplet size distribution.[12] However, strictly speaking, this formulation only works for homogeneous and isotropic turbulence (HIT). The flow in a stirred vessel is highly inhomogeneous and anisotropic, and bubbles/drops tend to shatter into tiny pieces if encountering strong shear region near the surface or tip of the impeller. The bubble breakup frequency and dynamics are not the same everywhere in the system, and they are sensitive to the design of the impeller and tank geometry.[13]

To overcome this problem, vertical water tunnels have been constructed in at least two research groups[14,15] prior to this work to study bubble dynamics in turbulence. Both of these tunnels have some interesting design features. One system has a rotating grid that was used not only to generate turbulence but also to create a large-scale vortex to trap bubbles near the centerline of the test section. Despite this rotating mean flow, flow exhibits a clear inertial range and seems to be homogeneous in the axial direction. ε in this system was not reported but can be estimated based on the fluctuation velocity u' and the integral length scale L, $\varepsilon \approx u'^3/L = 7 \times 10^{-3}$ m^2/s^3, which is much smaller than $O(0.1)$ m^2/s^3 that is needed. Although bubbles can still be deformed by turbulence when the local energy dissipation rate of the flow is significantly higher than its mean, the probability of bubbles encountering such strong local turbulence is rather low. The Twente Water Tunnel is another signature vertical water tunnel facility that has been used to study bubbles and light rigid particles. The system features an active grid that is used to generate turbulence. The active grid can increase the turbulence intensity and energy dissipation rate, but to a limit. In this system, as the mean flow increases from 0.22 m/s to 0.67 m/s, ε grows from 3.9×10^{-5} m^2/s^3 to 7.86×10^{-4} m^2/s^3. For the upper limit of ε, assuming the bubble size extends from 1 mm to 10 mm, We varies from 2.4×10^{-3} to 0.11, whereas Eo ranges from 0.13 to 13.6, nearly two orders-of-magnitude larger than We. This calculation suggests that, for deformable bubbles, the buoyancy-induced deformation (measured by Eo) dominates over the turbulence-induced deformation (measured by We). This difference only increases as the bubble size l_b grows since $Eo \propto l_b^2$ and $We \propto l_b^{5/3}$.

In addition to these two water tunnels, bubbles have also been studied in other facilities, e.g., the Twente Taylor-Couette system[16] for drag reduction. Bubbles in this system are clearly deformed.[16] Although the global-averaged energy dissipation rate is large,[16] $\varepsilon = 1.96$–13.5 m^2/s^3 (may even reach more than 180 m^2/s^3 based on the available cooling power[3]), most of it comes from the shear within two thin boundary layers. The bulk region that is closer to HIT condition has a much smaller energy dissipation rate from 10^{-4} to 1.[17] Bubble deformation in this system is affected by both the mean shear and the local turbulent fluctuations. To isolate the effect of turbulent fluctuations on bubble deformation and breakup, the mean shear is removed in our facility.

The passive grid or active grid methods, although standard for producing turbulence in water tunnels, are not adequate for producing turbulence with a large energy dissipation rate [$\varepsilon \geq O(0.1)$ m^2/s^3]. These methods rely on siphoning energy from the mean flow to drive turbulence, and only an extremely large mean flow can supply sufficient energy dissipation rate. A large mean flow is always problematic for optical diagnostics because bubbles often travel with the mean flow quickly in and out of the view area, creating a large statistical bias. To overcome this problem, we seek design inspirations from other turbulence facilities. In recent years, different mechanisms have been successfully used to generate HIT in a closed box. These mechanisms include injecting momentum into the system using oscillating grids,[18–20] propellers,[21] loudspeakers,[22,23] or jets.[24,25] Momentum is injected into the system from multiple symmetrical locations. The symmetry includes two facing planes,[24,25] eight corners of a cube[22,23] or polyhedrons.[21] It has been shown that planar injection produces HIT in a region that covers almost the entire cross section of the system.[24] The facing jet array design used in closed systems adopts a random forcing scheme by actuating jets randomly in space and in time.[24] The random forcing is designed to prevent the development of any persistent secondary flow in the system.[26]

The symmetric forcing using injections from multiple corners produces HIT confined in a small region at the center, and outside of this region, the flow recovers the characteristics specific to the way that the momentum is injected. Since turbulence decays as it moves away from the nozzle or loudspeaker, ε at the center is typically orders of magnitude lower than that near the injection point. As a result, the system features a low-ε core that is HIT but covered with a large shell of non-HIT with a much larger ε. If bubbles or droplets are introduced near the boundaries, they will be severely deformed or broken before even entering the HIT region. As a result, the only option is to inject bubbles or droplets directly into this region, but then the memory of injection could bias the statistics of bubble deformation and breakup as it is known that bubbles could experience a series of oscillations after detaching from a submerged needle even in a quiescent medium and it could be more complicated when there is background flow present or the needle is not perfectly aligned vertically.[27]

For our system, turbulence is driven by momentum jets coming from a plane. After some developing length, flow starts to become HIT within a thick slab that covers a large cross-sectional area. In a vertical water tunnel, the momentum injection plane should be placed at the top of the test section where ε is the strongest at about 4×10^4 m^2/s^3. As flow moves away from the injection plane into the test section, turbulence quickly decays and ε gets smaller and smaller. Bubbles are injected from the bottom of the test section where ε is the smallest. As bubbles rise, they experience flow with a growing ε, and their breakup probability starts to increase. The view area is set at a location where $\varepsilon > 0.1$ m^2/s^3, and bubbles with a few millimeters in size in this area will thus undergo strong deformation and breakup. This location is far away from the bubble injection point, and any memory of the injection will be lost by the time bubbles enter the view area. The ε mentioned above was calculated from the compensated second- and third-order structure functions; the details of the structure-function calculations along with other flow characteristics will be discussed later in Sec. IV.

II. EXPERIMENTAL APPARATUS

The new facility is constructed to meet three goals: (i) the system should be able to keep bubbles in the view area for an extended period of time; (ii) the system should generate turbulence that is nearly HIT over a large region; (iii) generated turbulence should have a large energy dissipation rate.

The experimental facility, V-ONSET (Vertical Octagonal Noncorrosive Stirred Energetic Turbulence), is designed to meet these goals (Fig. 1). The system is essentially a vertical water tunnel with an octagonal test section coupled with a jet array on the top of the test section. The system contains several subsystems: main flow loop, turbulence generator and controller, bubble/droplet bank, flow conditioning section, filtration, and other components. Each of the subsystems and their respective control mechanisms will be introduced and discussed in the following sections.

A. Main flow loop

V-ONSET is made of noncorrosive materials such as fiberglass, acrylic, and Polyvinyl chloride (PVC) for hosting purified and deionized water as well as salt water. In contrast to most water tunnel designs, the mean flow and turbulence can be controlled independently in V-ONSET. The main flow loop of the tunnel adopted a modular design such that each section can be swapped and connected in a different order to switch the mean flow direction between a downward and an upward configurations. This tunnel is designed for studying different types of multiphase flows, including light and heavy particles with different densities.

Driven by the buoyancy, the terminal rising velocity of bubbles u_s roughly scales with the size of bubbles as $u_s \propto \sqrt{l_b}$.[28] For light or heavy particles with diameter of a few millimeters rising in quiescent water, u_s is about 0.08–0.32 m/s.[28,29] In comparison, the fluctuation velocity $u' = \sqrt{(u_1'^2 + u_2'^2 + u_3'^2)/3}$ is about 0.04–0.24 m/s, which is of the same order of magnitude as the bubble rising terminal velocity in a quiescent medium. If there is no mean flow, bubbles or particles may exit the view area in the vertical direction faster than it

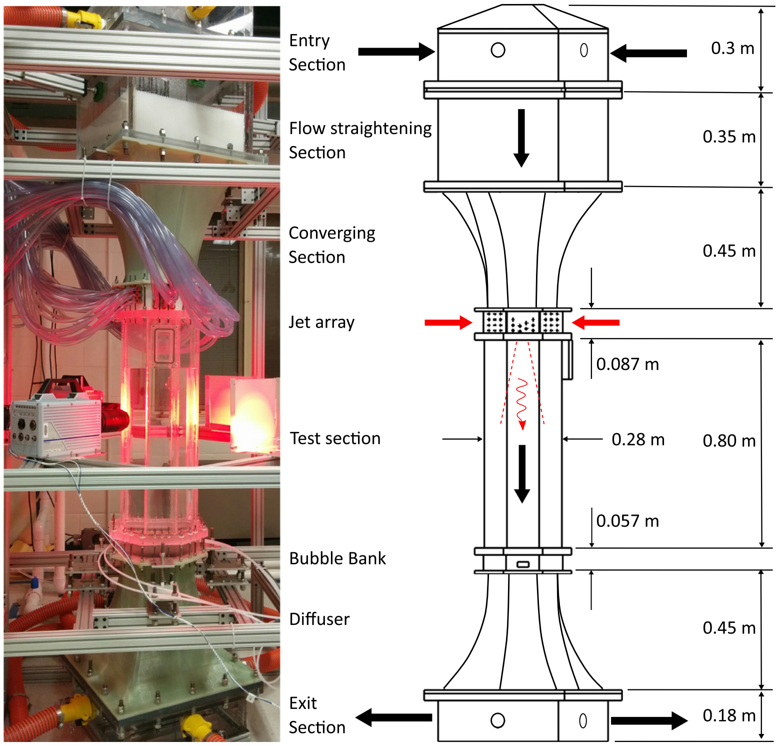

FIG. 1. Picture and schematic of different components of V-ONSET with the total height of 2.67 m.

would from the other two directions, which may lead to biased statistics. To avoid this finite-view-area effect, the mean flow along the vertical direction $\langle u_3 \rangle$ is adjusted to match u_s but in the opposite direction.

Most existing wind/water tunnel designs take a large footprint because the return loop has almost the same cross-sectional area as the main section to reduce the pressure drop and maximize the flow rate. In our system, the mean flow is used only to suspend bubbles not to drive turbulence, so it was kept at a low value. This allows us to reduce the size of the return loop significantly. The return section is made of 5.1 cm-diameter PVC pipe. When the cross-sectional size reduces from 23 cm at the test section to 5.1 cm at the return loop, the pressure drop per unit length increases by 1865.5 times. But the pump can still afford this increase of pressure because of the low flow rate.

When only the mean flow is turned on, bubbles of millimeter in size stop rising up in the test section. Bubbles that are much larger will still be able to rise through the view area, although at a reduced velocity. Much smaller bubbles will be flushed with the mean flow to the bottom of the main loop and back to the top of the tunnel through the return loop. At the top of the tunnel, there is a large mixing tank with a cone-shaped top that is used to trap bubbles, force them to merge, and release them back to the air. The mean flow essentially acts as a filter to select bubbles of certain size based on their rising velocity. The interesting part is that bubbles staying in the test section do not freeze completely. They jiggle around at a relatively fixed location. This motion is likely due to bubbles' unsteady wake dynamics,[30] which tend to drive bubbles to follow a spiraling or zigzagging trajectory when they rise up. Such a motion becomes a local jiggling motion in our case as the mean flow essentially moves the lab reference frame with the bubble mean rising velocity.

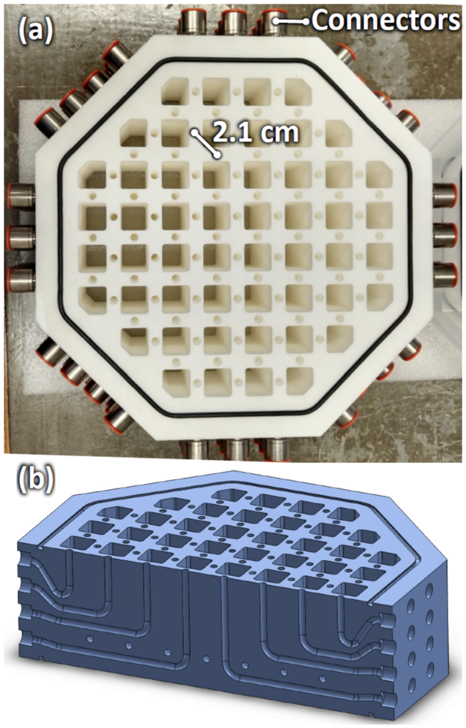

FIG. 2. (a) Picture of the 3D printed jet array with both large square through holes and small jet nozzles, as well as a black O-ring and push-to-connect fittings on the side. (b) A 3D schematic of the jet array showing the inlet holes on side walls which are connected to their respective outlet holes on the top surface through internal channels. It also shows square openings across the structure that allow mean flow to pass through it.

B. Turbulence generator and controller: High-speed jet array

The mean flow and the turbulence control loop are divided after the pump but later reunited in the test section using a jet array, which is the heart of the entire V-ONSET. As shown in Fig. 2(a), the jet array looks like a bar grating. 88 circular nozzles of 5 mm in diameter are positioned in a staggered pattern with 2.1 cm apart from each other on the bottom surface of the jet array. These nozzles are used to inject high-speed water jets into the test section coaxially with the mean flow. The turbulence characteristics are generated and controlled by the speed of these high-speed jets (up to 12 m/s). In addition to these nozzles, 52 square through holes with a cross-sectional area of 2×2 cm^2 are left for the mean flow to pass. The length of these through holes is 8.7 cm, same as the thickness of the jet array. Downstream of the jet array, the jets and the mean flow merge together, producing turbulence with a low mean flow and high turbulence intensity.

The jet nozzles are connected to the side openings through internal channels, as shown in the cutaway view in Fig. 2(b). Note that there are seven holes near the bottom of the cutaway plane, which indicates another seven internal channels going perpendicular to this plane. The arrangement of all internal channels is designed based on three principles: (a) Before flow exits the nozzle, there has to be a sufficiently long (six nozzle diameter) vertical section to ensure a straight coaxial jet. (b) Inlets are distributed evenly on eight side walls, shown as the red connectors in Fig. 2(a). (c) Every nozzle needs to be connected to a dedicated inlet on the closest wall. This design features two key flow isolations: the square through holes for the mean flow and the internal channels for the jets are separated, and the individual channel for each jet separates jets from each other. The minimum wall thickness of each nozzle is set at 2.5 mm to make sure that the high-pressure water does not leak through different channels.

Due to the complexity of 88 curved internal channels stretched around 52 square through holes, we decided to use the additive manufacturing (so-called 3D printing) method to construct the jet array. Many methods have been tested, and most extrusion-based methods did not offer water-proof build even at a very low material porosity (high material density). The metal powder Selective-Laser-Sintering (SLS) process is too expensive for a structure at this large scale. After several iterations, the best option is to use PA12 polyamide 60 μm diameter powders fused together through the SLS process. The printed structure is water proof with around 48 MPa maximum tensile strength based on the ASTM D638 standard. Note that the material strength is so high that the jet array can handle a much higher pressure than what the system was operated at.

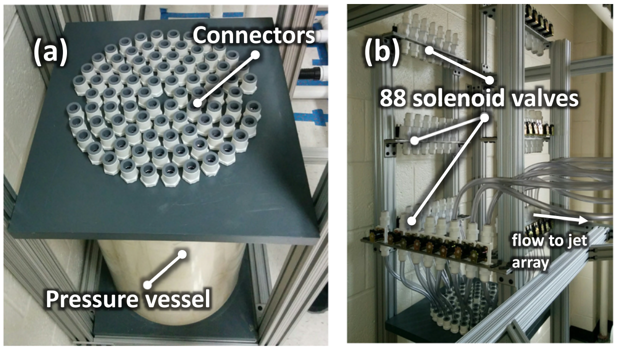

FIG. 3. (a) Pressure manifold and (b) solenoid valves used to control the high speed water jets used for generating turbulence in the test section.

As shown in Fig. 3, each nozzle in the jet array is controlled by a dedicated solenoid valve that opens and closes the jet from a common pressure vessel. The pressure vessel features a cylindrical storage tank with an outer diameter of 0.36 m and a wall thickness of 9.5 mm. The top end of the vessel is covered with a 0.05 m thick PVC plate and fitted with 88 outlets. The bottom of the vessel is also sealed with a PVC plate and fitted with a 0.051 m-diameter pipe as the inlet. Given the large pressure surges caused by the frequent switching on-off of jets, the inlet is connected to a variable pressure release valve to mitigate the water hammering problem.

The key difference between our jet array design and many previous versions driven by submerged pumps[24,26,31] is that the jet velocity u_{jet} can be much larger. For example, in our current configuration, the record of u_{jet} is 12 m/s from each nozzle, and it can be pushed even higher as long as our pressure vessel can withstand the pressure. For our purpose, at least for now, 10–12 m/s jet velocity is sufficient. Another benefit is that every jet is a momentum jet by design. Water supply of these jets comes from upstream of the jet array. When a jet is fired down into the test section, the incompressible water forces the same amount of water to be taken away from exactly the same plane through those square through holes. Most other jet array systems that rely on submerged pumps do not necessarily have the suction end and nozzles colocated at the same plane, potentially resulting in some small amount of mass flux. In our system, this zero mass flux is inherent to the design and guaranteed.

Although the net mass flux is zero, each jet does not follow a classical synthetic jet profile.[32] In our system, the mass is taken away uniformly from these square through holes across the entire cross section, which is different from the alternating momentary ejection and suction of fluid across an orifice as used in classical synthetic jets.[33] The Reynolds number of each jet produced by our jet array, based on the jet velocity of 12 m/s, is about $Re = 6 \times 10^4$, which is well into the turbulence regime.

For the turbulent round jet, in the near field, most kinetic energy is contained within the mean flow. In the far field ($x/d > 15$), as the kinetic energy continues to transfer from the mean flow to the turbulent fluctuations, the jet half-width $R_{1/2}$ grows linearly as a function of the streamwise coordinate x as $R_{1/2}(x)/d = K_d(x - x_p)/d$, where x_p is the virtual jet origin and K_d is about 0.1.[34] At this large Reynolds number ($Re > 50\,000$), after scaling with the jet width, the jet profile should be self-similar (self-preserve).[35] The energy dissipation rate can be as large as 2000 m^2/s^3 at $x/d = 15$ away from the nozzle.[36] As x/d increases, ε drops quickly. For the view volume located at 38 cm ($x/d = 76$) away from the jet array, the half width of the jet grows close to 3.8 cm, which is larger than the jet spacing of 2.1 cm. This suggests that, at this distance, jets are likely to be fully mixed with each other and also with the background turbulence. At the same time, most of the kinetic energy has been converted from the mean flow to the turbulent fluctuations. Even though ε reduces to 0.16 m^2/s^3, the view volume is still chosen at this location to make sure that any dynamics seen in our system is driven by HIT rather than turbulent jets. Ideally, we would like to vary the distance between the view area and the jet array. But the six-camera optical configuration that we designed to reconstruct the complex shapes of deformable bubbles in the tunnel becomes too heavy and cumbersome to move up and down. The view-volume-to-nozzle distance has been kept constant so far.

Each jet is controlled by a solenoid valve, which can be switched on and off by a relay board. The relay board is controlled by a LabView code that programs the on-off time of each nozzle. The system allows us to open all 88 nozzles if necessary, but so far we have not tried to open all the jets because opening only 11 jets on average is sufficient to provide a large energy dissipation rate.

The spatial-temporal jet driving pattern is similar to what has been used in other jet array systems.[24,31] The probability of each jet being on is 12.5%. The total number of open jets at any given time follows a Gaussian distribution (mean $\mu = 11$ and standard deviation $\sigma = 3$). Each random pattern lasts for 3 s. During experiments, pressure surges caused by water hammering are not as dangerous as turning off too many jets suddenly. For most following studies, the control system forbids the number of jets at any time from going below nine because one pressure vessel broke after turning off too many jets.

C. Bubble/droplet bank

A bubble bank is an octagonal structure located right below the test section. As shown in Fig. 4, it is composed of two structures: (i) a base that is used to connect to the tunnel [Fig. 4(a)] and (ii) a gas flow distributor that uniformly sends air through four independently controlled islands of hypodermic needles to generate bubbles [Fig. 4(b)]. The base and gas flow distributor are connected and sealed using nylon screws and an O-ring, rather than using permanent glue. This design allows us to easily switch capillary islands for different experiments as the island that is used for oil with surfactants cannot be reused for gas bubble injection.

Another unique part of our design is that the gas flow distributor is designed like a shower head with five layers of structures to distribute flow from an individual inlet to an array of needles uniformly. Out of the total four islands, two of them contain gauge 25 (inner diameter: 160 μm, outer diameter: 300 μm) needles, whereas the other two house gauge 30 (inner diameter: 260 μm, outer diameter: 500 μm) needles. These needles are permanently glued to the acrylic plate using plastic-steel glue. The bubble/droplet bank allows us to inject bubbles or oil droplets with a wide size distribution by adjusting the needle gauge and the flow rate through the needles.

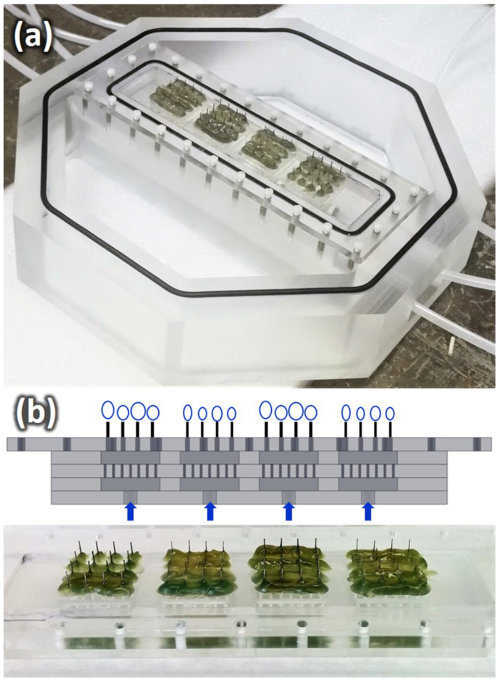

FIG. 4. (a) Bubble bank base housing the gas flow distributor. (b) Closer look at the capillary island fitted with hypodermic needles and five-levels gas distributing system.

D. Flow conditioning section

To maintain a relatively uniform mean flow in the test section, the flow needs to be conditioned to remove as much of the secondary flow generated from other parts of the tunnel as possible. The largest source of the uncontrolled secondary flow is at the top mixing tank. Immediately downstream of this mixing tank, a pressure plate with many small holes is used to redistribute the pressure uniformly across the entire cross section and reduce the secondary flow. The flow straightening section that holds a honeycomb structure is connected to the pressure plate to force the flow to become laminar.

Downstream of the settling chamber, the contraction section with a 4:1 contraction ratio (Fig. 5) further reduces the secondary flow by stretching vortices that survived after the honeycomb structures. The other key purpose of the contraction section is to convert the cross-sectional geometry. The octagonal design of the test section posed many manufacturing challenges. If we had to maintain this geometry throughout the entire water tunnel, the problem would escalate and the cost of the tunnel would increase probably by a factor of two. The contraction section was designed to convert the cross section from a squared geometry to an octagonal geometry. The structure also has flanges at both ends to connect to other tunnel components.

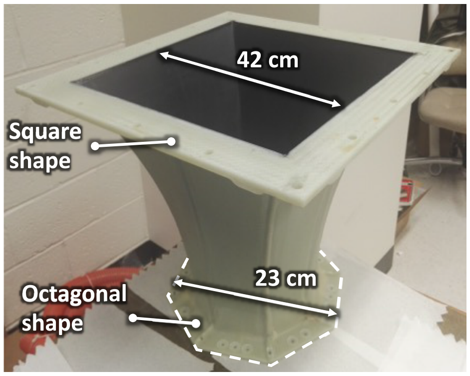

FIG. 5. Contraction section made of fiber glass.

E. Filtration and other components

For bubbles/droplets, the interfacial contamination could change the dynamics significantly. The water purification system has to be very efficient and capable of producing a large amount of water overnight. V-ONSET has a dedicated water purification system, which is a three-stage water purification system that can provide type II purified water. The purification system can produce purified water at 7 l/h. One night before experiments, the purified water would be produced and stored in the tank. The water would also be degassed by connecting the tank to a vacuum pump.

The flow circuit of V-ONSET contains two pumps—a large 7.46 kW three-phase pump and a smaller 1.12 kW three-phase pump. Both pumps offer some advantages compared with each other. The large one is a high flow rate pump with a maximum flow rate of 0.016 m^3/s and a maximum pressure of 561.8 kPa. This pump is used as the main energy source to create both the mean flow and high-speed water jets. The small pump can provide a maximum flow rate of 3.8×10^{-3} m^3/s and a maximum pressure of 328.4 kPa, which serves as an auxiliary pump that is mainly used for filtration and filling the tunnel. Water in the tunnel also needs to be regularly filtered and sanitized. For example, high concentrations of tracer particles need to be removed from the system using two sedimentation filters that can allow flow rates up to 6×10^{-4} m^3/s withstanding a maximum pressure drop of 275.8 kPa. This filter cannot keep up with the minimum flow rate supplied by the large pump. So, the small pump is used to circulate water through the filters. In addition to filters, a UV system was also connected to remove any bacteria growing in the system.

III. IMAGING SYSTEM

A. Octagonal test section

Figure 6 shows the test section of the tunnel, which is 80 cm tall and 23 cm in diameter as an inscribed circle. The tank is made of 25.4 mm thick acrylic sheet for optical access. The facility was designed to study the 3D complex deformation and breakup dynamics of bubbles or droplets in strong turbulence. The octagonal test section was selected because we would like to have cameras covering the entire perimeter of the test section from different directions. In addition, an octagonal test section helps avoid using the liquid-filled prisms that typically limit the view volume.

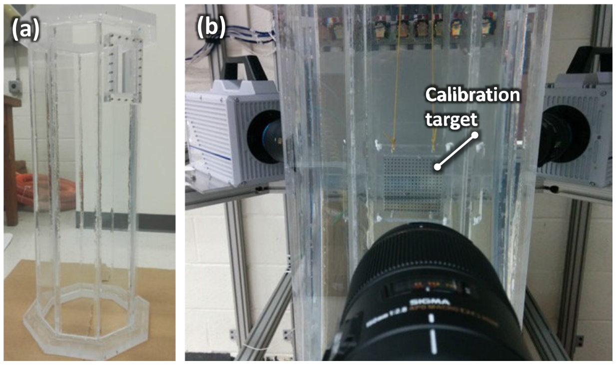

FIG. 6. (a) Picture of the 80 cm long octagonal test section. It also shows a window on one of the faces to insert a calibration target. (b) Three of the total six cameras look at a transparent target with an array of dots with known positions in the center of our view area.

To image the dispersed phase, backlighting is selected because it is the best to generate sharp images of bubbles/droplets[37] without inducing strong reflection. The imaging system was designed to achieve simultaneous measurements of both phases. The system consists of six high speed cameras, rather than four that is typically adopted in fluid dynamics community, for two reasons: (i) reconstructing bubble deformation with a large degree of freedom requires more than four views. A six-camera configuration is chosen to maximize the ratio between the benefit measured by the reconstruction fidelity to the total cost. (ii) Finite-size bubbles tend to block views of tracer particles behind them. Six cameras are needed for maximizing the opportunity for more than three cameras to simultaneously view tracer particles close to bubbles without being shadowed.

Figure 7 shows the camera configuration. Cameras need to be positioned to cover as many orthogonal views as possible. In practice, camera views are limited by the tunnel configuration and illumination designs. For example, in our system, the vertical tunnel design forbids cameras from accessing the top or the bottom view of the interrogation volume because cameras cannot be put into the test section. To mitigate this problem, two cameras (Cam 3 and Cam 5) are tilted to provide some information in the vertical direction. To keep the integrity of the tunnel, no liquid prisms were used for these two cameras, so the tilted angle is small (22°) to avoid refraction-led uncertainty.

The diffused LED light is used to illuminate the deformable dispersed particles from the back.[37] The carrier phase is seeded with polyamide tracer particles for performing Lagrangian particle tracking.[38] These particles have a nominal radius a of 30 μm with density close to 1.03 g/cm^3. The particle response time τ_p [$\tau_p = 2a^2\Delta\rho/(9\nu\rho_f)$] is approximately 6 μs; The Kolmogorov time τ_η ($\tau_\eta = \sqrt{\nu/\varepsilon}$) is about 2.2–3.5 ms. The ratio of these two timescales leads to the Stokes number, which is much smaller than unity for these particles ($St = \tau_p/\tau_\eta \ll 1$),[39] indicating that these particles can be safely treated as tracers. It has also been shown that adding tracers has a negligible effect on bubble rising velocity (less than 1%) as compared to that in pure water.[40,41] This helps justify that adding particles may not alter the interfacial dynamics significantly, but the contamination of the interface is possible and cannot be completely ruled out.

IV. EXAMPLE OF FLOW MEASUREMENT

Prior to experiments, tracer particles were injected into the system through the mixing tank at the top. Tracers get quickly mixed with water and transported down into the test section. The concentration was kept low in the very beginning of our experiments to improve the calibration results. After this procedure, the concentration was gradually increased until the number of particles on 2D images reaches 10 000–20 000 for our cameras with one megapixel resolution. Since the back illumination was used, the shadows of tracer particles were projected onto the imaging planes of all six cameras. The images were then inverted to have bright particles in front of a dark background. Most tracer particles appeared to have three to five pixels in diameter on images. Their positions were triangulated and tracked over time using our in-house STB code.[42] The code was parallelized to run on the Maryland Advanced Research Computing Center (MARCC). For each experiment, the raw images were uploaded to MARCC and simple image preprocessing was done. Particles were then tracked, and their trajectories were stored in a binary file. MARCC allows us to run multiple

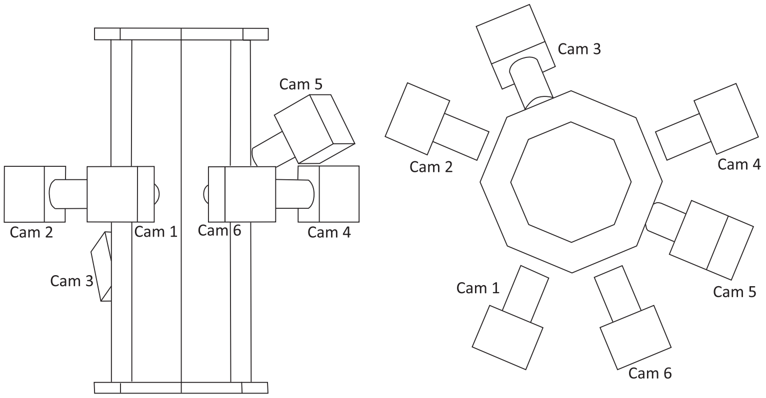

FIG. 7. Schematic of six high speed cameras positioned around the octagonal test section of V-ONSET including (left) the side view and (right) the top view.

TABLE I. Controllable parameters and turbulence characteristics.

Controllable parameters				Turbulence characteristics					
$N_{jets,total}$	$\langle N_{jets,on}\rangle$	u_{jet} (m/s)	$\langle u\rangle$ (m/s)	u' (m/s)	ε (m^2/s^3)	$Re_\lambda = \sqrt{15u'L/\nu}$	$L = u'^3/\varepsilon$ (cm)	τ_η (ms)	η (μm)
88	11	2.455	0.1965	0.0383	0.001 25 ± 0.000 23	160 ± 15	4.49 ± 0.8	28.3 ± 2.5	168 ± 7
88	11	11.92	0.2322	0.2122	0.16 ± 0.02	435 ± 20	5.97 ± 0.70	2.5 ± 0.15	50 ± 1.5

jobs at one time, which significantly improves the speed of our data analysis.

Table I shows two examples of the flow regime that can be achieved in this system, one with the lowest jet velocity and the other one with the highest jet velocity. Both flow configurations have identical total number of jets $N_{jets,total}$ as well as the average number of open jets $\langle N_{jets,on}\rangle$. As one can see, as the jet velocity increases, the fluctuation velocity increases proportionally as well. Since ε scales with u' to its third power, it is not surprising that ε increases by two orders of magnitude with the maximum one exceeding 0.1 m^2/s^3. In addition, the Taylor-scale Reynolds number, $Re_\lambda = \sqrt{15u'L/\nu}$, is also seen to grow as the jet velocity increases with the maximum one reaching $Re_\lambda = 435 \pm 20$.

For each experiment, all particle trajectories in the entire view volume of roughly 6 cm × 6 cm × 5 cm were used. Figure 8 shows the velocity profile, including both the mean $\langle u_i\rangle$ and the fluctuation components u_i', in the horizontal and vertical directions. The error bar indicates the variation of these quantities in other directions. $\langle u_i\rangle$ and u_i' are relatively uniform in both directions. In particular, the horizontal fluctuations are significantly stronger than the mean which are close to zero. In the vertical direction, the fluctuation velocity does not show a strong trend, but it is not as flat as two other directions. In particular, it shows a weak decay in the vertical direction as it moves away from the jet array (positive Z is closer to the jet array). This is consistent with what one would expect that turbulence should decay as it moves away from the energy injection. For this particular configuration, the decay rate seems to be slow.

One important design goal is to have strong turbulence with a large energy dissipation rate $\varepsilon \geq 0.1$ m^2/s^3. This is to assure that the turbulence-induced deformation is stronger than the buoyancy-induced one $We \geq Eo \geq 1$. To estimate the energy dissipation rate in our system, the Eulerian velocity structure function $D(r) = \langle (u(x + r) - u(x))^2\rangle$ is calculated based on the Lagrangian particle trajectories as introduced in a previous study.[43]

In this work, the spatial resolution is not sufficient to resolve the dissipative range ($r \ll \eta$) below the Kolmogorov scale η. But the scales in the inertial range ($\eta \ll r \ll L$, $L \approx 400\eta$) are well resolved. Based on the Kolmogorov theory, in the inertial range, the structure function should only depend on the energy dissipation rate and the scale separation r. The longitudinal D_{LL} and transverse D_{NN} components of the second-order structure function can be related to ε and r as $D_{LL} = C_2(\varepsilon r)^{2/3}$ and $D_{NN} = 4C_2(\varepsilon r)^{2/3}/3$ ($C_2 \approx 2.3$[44]). In Fig. 9(a), both D_{LL} and D_{NN} are shown as a function of r, and the solid line indicates the $r^{2/3}$ scaling in the inertial range. In addition, the four-fifths law of the Kolmogorov theory suggests that the third-order structure function in the inertial range follows $D_{LLL} = -4\varepsilon r/5$. Compensated by their respective inertial range scalings and prefactors, all three structure functions can be used to estimate ε. In Fig. 9(b), three compensated structure functions are shown together. A perfect collapse between D_{LL} and D_{NN} confirms that (i) flow is close to HIT and (ii) turbulence in this region is fully developed and has a reasonably wide inertial range for our Reynolds number at $R_\lambda \approx 435$. In addition, the compensated third-order structure function is also shown, which shows a plateau in a range that is similar with D_{LL} and D_{NN}. The heights of three plateaus agree with each other very well. The energy dissipation rate for this particular test case can be estimated to be

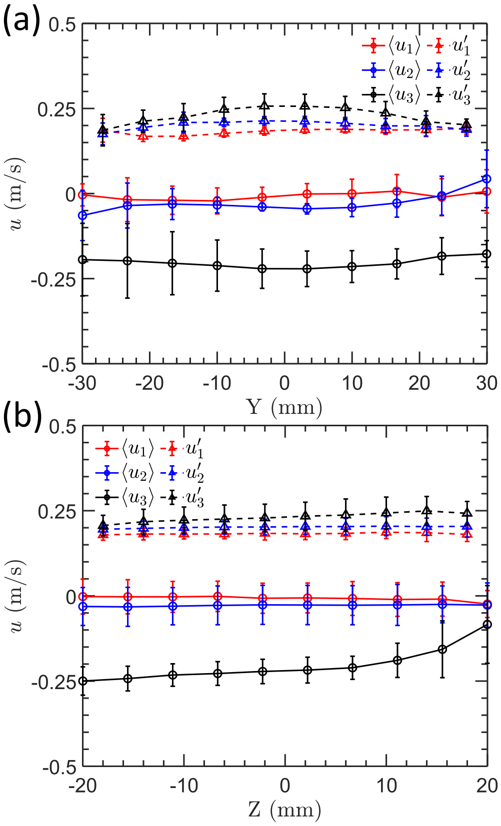

FIG. 8. The mean and fluctuation velocity ($\langle u_i\rangle$ and u_i', i = 1, 2, 3 for three axes) are plotted as a function of (a) the horizontal axis (Y) and (b) the vertical axis (Z). The error bar indicates the standard deviation of the velocity in other directions.

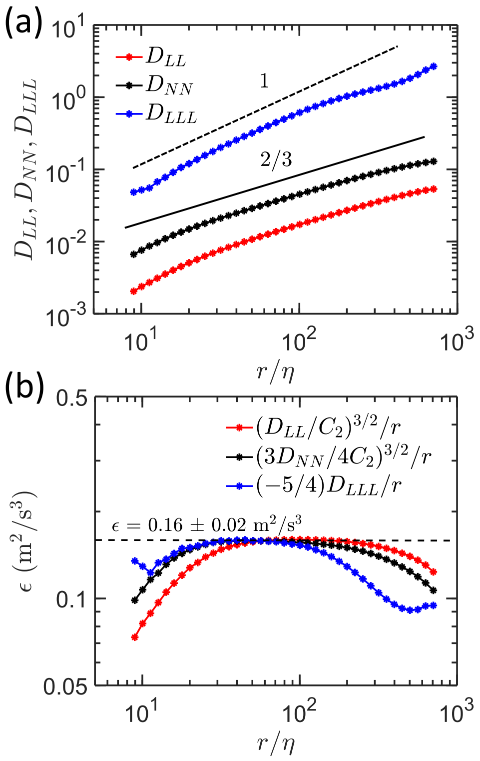

FIG. 9. (a) The second-order longitudinal (D_{LL}) and transverse (D_{NN}) structure functions as well as the third-order longitudinal structure functions (D_{LLL}) as a function of scale separation r. The dashed line indicates r^1, and the solid line shows $r^{2/3}$. (b) Energy dissipation rate ε (m^2/s^3) estimated by structure functions compensated by their respective scaling laws. The plateau height can be used to estimate ε.

around 0.16 ± 0.02 m^2/s^3. The uncertainty of ε is estimated to cover the difference among three structure functions. ε is in the range that is required to have bubble deformation significantly driven by turbulence.

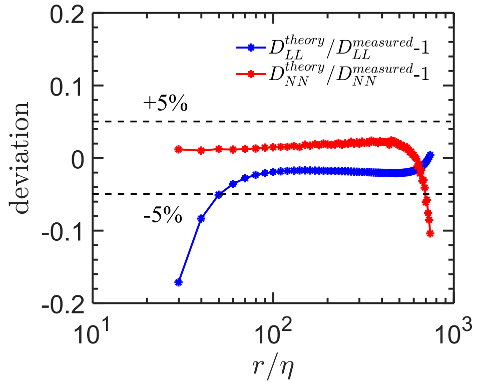

FIG. 10. The deviation between the measured and calculated second-order longitudinal (D_{LL}) and transverse (D_{NN}) structure functions vs length scale r. The calculated structure functions are obtained from Eqs. (1) and (2).

The statistically isotropic turbulence follows the Kármán-Howarth equation,[45] and it can be expressed as a relationship between the longitudinal and transverse second-order structure functions,

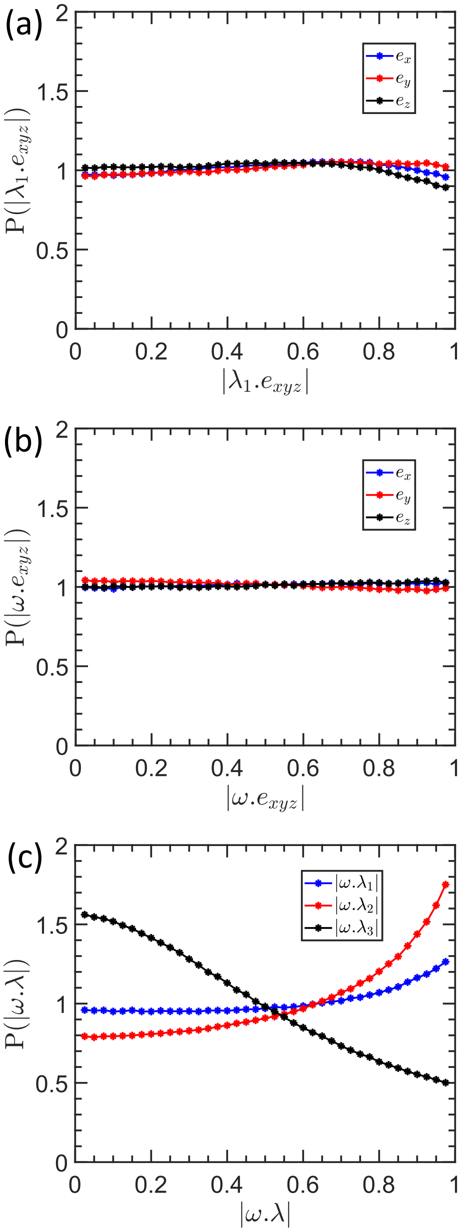

FIG. 11. Alignment of (a) λ_1 of the coarse-grained velocity gradient tensor with the main axes of the lab frame of reference, (b) coarse-grained vorticity vector alignment with the with the main axes of the lab frame of reference, and (c) PDF of the alignment between vorticity unit vector and the three eigenvectors of the coarse-grained rate-of-strain tensor showing a preferential alignment between vorticity vector and the intermediate eigenvector of the rate-of-strain tensor which is characteristic of isotropic turbulence.

$$D_{NN}(r) = D_{LL}(r) + \frac{r}{2}\frac{\partial D_{LL}(r)}{\partial r}, \tag{1}$$

and its reverse form,

$$D_{LL}(r) = \frac{2}{r^2}\int_0^r x D_{NN}(x)dx. \tag{2}$$

As it has been shown before,[21] these two equations help calculate D_{LL} and D_{NN} from the experimental results of D_{NN} and D_{LL}, respectively. The measured structure functions are shown in Fig. 9. The deviation between the measured structure function and the calculated one can be obtained, and this deviation measures the validity of the isotropic assumption. As shown in Fig. 10, the deviation between the calculation and experimental measurements is less than 5% for the length scales in the range of $[50\eta, 500\eta]$, indicating that the turbulence is close to homogeneous and isotropic within the inertial range.

The statistical isotropy can also be tested by evaluating the coarse-grained velocity gradient tensor. The entire view volume was divided into small cubes of 8 mm in size to calculate the local coarse-grained velocity gradient tensor. Each measured tensor was decomposed into the vorticity vector and rate-of-strain tensor. For statistically isotropic turbulence, the orientations of the vorticity vector $\boldsymbol{\omega}$ and the three eigenvectors of the rate-of-strain tensor λ_i $(i = 1, 2, 3)$ are supposed to be random in space. Figure 11 shows the PDFs of the cosine of the angles between (a) $\boldsymbol{\omega}$ and (b) $\boldsymbol{\lambda}_1$ with three principal axes of the lab reference of frame. The uniform distribution in both PDFs implies that turbulence generated in this facility is close to isotropic. To confirm that this calculation is not an artifact, the PDF of the alignment between the vorticity vector and the three eigenvectors of the strain rate tensor are also shown in Fig. 11(c). The results show that the vorticity is preferentially aligned with the intermediate eigenvector of the rate-of-strain tensor. This is due to the delayed alignment between the flow stretching and the vorticity vector.[46] This result confirms that our calculation of the coarse-grained velocity gradient tensor is correct, and the flow is indeed close to isotropic.

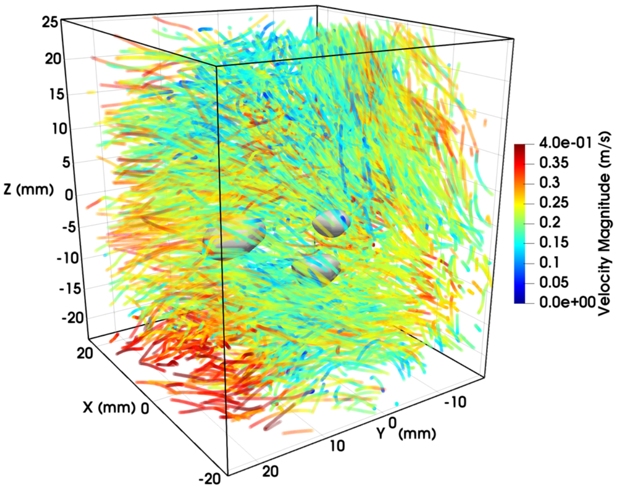

FIG. 12. Reconstructed bubbles (gray blobs) with surrounding tracer particle trajectories color coded by their velocity magnitude.

The single-phase measurement confirms that the flow characteristics satisfy our design goals. Within this flow, bubbles experience strong turbulence that is close to HIT. This will help us to collect the statistics of bubble dynamics and two-phase couplings in a condition that is relevant to applications with strong background turbulence. In Fig. 12, an example of the two-phase flow measurements is shown. The trajectories of tracers around bubbles are shown as lines color-coded with their respective velocity magnitude. These lines are set with a certain level of transparency to show bubbles within. The 3D geometry of bubbles is shown as gray blobs. In this particular case, bubble deformation is not very strong. With six high-speed cameras coupled with a new reconstruction algorithm, the bubble geometry is acquired at an unprecedented accuracy. The center-of-mass of bubbles can also be tracked in a similar way using our particle tracking code. This facility offers us a unique opportunity to study the bubble-turbulence couplings in both Eulerian and Lagrangian frameworks.

ACKNOWLEDGMENTS

We acknowledge the help of Jhi Loke Yong, Chee Hau Teoh, Gokhan Akarsalan, and Yilun Zhang. This study was financially supported by the National Science Foundation under the Award Nos. 1705246 and CAREER-1653389.

REFERENCES

[1] F. König, E.-S. Zanoun, E. Öngüner, and C. Egbers, "The CoLaPipe—The new Cottbus large pipe test facility at Brandenburg University of Technology Cottbus-Senftenberg," Rev. Sci. Instrum. **85**, 075115 (2014).

[2] A. La Porta, G. A. Voth, A. M. Crawford, J. Alexander, and E. Bodenschatz, "Fluid particle accelerations in fully developed turbulence," Nature **409**, 1017 (2001).

[3] D. P. van Gils, G.-W. Bruggert, D. P. Lathrop, C. Sun, and D. Lohse, "The twente turbulent Taylor–Couette (T^3C) facility: Strongly turbulent (multiphase) flow between two independently rotating cylinders," Rev. Sci. Instrum. **82**, 025105 (2011).

[4] D. P. Lathrop, J. Fineberg, and H. L. Swinney, "Turbulent flow between concentric rotating cylinders at large Reynolds number," Phys. Rev. Lett. **68**, 1515 (1992).

[5] F. Ravelet, R. Delfos, and J. Westerweel, "Influence of global rotation and Reynolds number on the large-scale features of a turbulent Taylor–Couette flow," Phys. Fluids **22**, 055103 (2010).

[6] M. Hultmark, M. Vallikivi, S. Bailey, and A. Smits, "Turbulent pipe flow at extreme Reynolds numbers," Phys. Rev. Lett. **108**, 094501 (2012).

[7] E. Bodenschatz, G. P. Bewley, H. Nobach, M. Sinhuber, and H. Xu, "Variable density turbulence tunnel facility," Rev. Sci. Instrum. **85**, 093908 (2014).

[8] E. M. King and J. M. Aurnou, "Turbulent convection in liquid metal with and without rotation," Proc. Natl. Acad. Sci. U. S. A. **110**, 6688–6693 (2013).

[9] C. M. White, A. N. Karpetis, and K. R. Sreenivasan, "High-Reynolds-number turbulence in small apparatus: Grid turbulence in cryogenic liquids," J. Fluid Mech. **452**, 189–197 (2002).

[10] A. N. Kolmogorov, "The local structure of turbulence in incompressible viscous fluid for very large Reynolds numbers," Dokl. Akad. Nauk SSSR **30**, 299–303 (1941).

[11] J. Hinze, "Fundamentals of the hydrodynamic mechanism of splitting in dispersion processes," AIChE J. **1**, 289–295 (1955).

[12] S. Maaß, F. Metz, T. Rehm, and M. Kraume, "Prediction of drop sizes for liquid–liquid systems in stirred slim reactors, Part I: Single stage impellers," Chem. Eng. J. **162**, 792–801 (2010).

[13] G. Zhou and S. M. Kresta, "Impact of tank geometry on the maximum turbulence energy dissipation rate for impellers," AIChE J. **42**, 2476–2490 (1996).

[14] F. Ravelet, C. Colin, and F. Risso, "On the dynamics and breakup of a bubble rising in a turbulent flow," Phys. Fluids **23**, 103301 (2011).
[15] J. M. Mercado, V. N. Prakash, Y. Tagawa, C. Sun, D. Lohse, and (International Collaboration for Turbulence Research), "Lagrangian statistics of light particles in turbulence," Phys. Fluids **24**, 055106 (2012).
[16] D. P. van Gils, D. N. Guzman, C. Sun, and D. Lohse, "The importance of bubble deformability for strong drag reduction in bubbly turbulent Taylor–Couette flow," J. Fluid Mech. **722**, 317–347 (2013).
[17] R. Ezeta, S. G. Huisman, C. Sun, and D. Lohse, "Turbulence strength in ultimate Taylor–Couette turbulence," J. Fluid Mech. **836**, 397–412 (2018).
[18] I. De Silva and H. Fernando, "Oscillating grids as a source of nearly isotropic turbulence," Phys. Fluids **6**, 2455–2464 (1994).
[19] E. Villermaux, B. Sixou, and Y. Gagne, "Intense vortical structures in grid-generated turbulence," Phys. Fluids **7**, 2008–2013 (1995).
[20] A. Srdic, H. Fernando, and L. Montenegro, "Generation of nearly isotropic turbulence using two oscillating grids," Exp. Fluids **20**, 395–397 (1996).
[21] R. Zimmermann, H. Xu, Y. Gasteuil, M. Bourgoin, R. Volk, J.-F. Pinton, E. Bodenschatz, and I. C. for Turbulence Research, "The Lagrangian exploration module: An apparatus for the study of statistically homogeneous and isotropic turbulence," Rev. Sci. Instrum. **81**, 055112 (2010).
[22] M. Birouk, B. Sarh, and I. Gökalp, "An attempt to realize experimental isotropic turbulence at low Reynolds number," Flow, Turbul. Combust. **70**, 325–348 (2003).
[23] W. Hwang and J. Eaton, "Creating homogeneous and isotropic turbulence without a mean flow," Exp. Fluids **36**, 444–454 (2004).
[24] G. Bellani and E. A. Variano, "Homogeneity and isotropy in a laboratory turbulent flow," Exp. Fluids **55**, 1646 (2014).
[25] D. Carter, A. Petersen, O. Amili, and F. Coletti, "Generating and controlling homogeneous air turbulence using random jet arrays," Exp. Fluids **57**, 189 (2016).
[26] E. A. Variano, E. Bodenschatz, and E. A. Cowen, "A random synthetic jet array driven turbulence tank," Exp. Fluids **37**, 613–615 (2004).
[27] H. N. Oguz and A. Prosperetti, "Dynamics of bubble growth and detachment from a needle," J. Fluid Mech. **257**, 111–145 (1993).
[28] M. Wu and M. Gharib, "Experimental studies on the shape and path of small air bubbles rising in clean water," Phys. Fluids **14**, L49–L52 (2002).
[29] M. A. R. Talaia, "Terminal velocity of a bubble rise in a liquid column," World Acad. Sci. Eng. Technol. **28**, 264–268 (2007).
[30] P. Ern, F. Risso, D. Fabre, and J. Magnaudet, "Wake-induced oscillatory paths of bodies freely rising or falling in fluids," Annu. Rev. Fluid Mech. **44**, 97–121 (2012).
[31] E. A. Variano and E. A. Cowen, "A random-jet-stirred turbulence tank," J. Fluid Mech. **604**, 1–32 (2008).
[32] B. L. Smith and A. Glezer, "The formation and evolution of synthetic jets," Phys. Fluids **10**, 2281–2297 (1998).
[33] A. Glezer and M. Amitay, "Synthetic jets," Annu. Rev. Fluid Mech. **34**, 503–529 (2002).
[34] T. G. Malmström, A. T. Kirkpatrick, B. Christensen, and K. D. Knappmiller, "Centreline velocity decay measurements in low-velocity axisymmetric jets," J. Fluid Mech. **346**, 363–377 (1997).
[35] S. B. Pope, *Turbulent Flows* (Cambridge University Press, 2000).
[36] C. Martínez-Bazán, J. Montanes, and J. C. Lasheras, "On the breakup of an air bubble injected into a fully developed turbulent flow. Part 1. Breakup frequency," J. Fluid Mech. **401**, 157–182 (1999).
[37] A. Jordt, C. Zelenka, J. S. von Deimling, R. Koch, and K. Köser, "The bubble box: Towards an automated visual sensor for 3D analysis and characterization of marine gas release sites," Sensors **15**, 30716–30735 (2015).
[38] R. Ni, S. Kramel, N. T. Ouellette, and G. A. Voth, "Measurements of the coupling between the tumbling of rods and the velocity gradient tensor in turbulence," J. Fluid Mech. **766**, 202–225 (2015).
[39] M. Raffel, C. E. Willert, F. Scarano, C. J. Kähler, S. T. Wereley, and J. Kompenhans, *Particle Image Velocimetry: A Practical Guide* (Springer, 2018).
[40] R. Lindken and W. Merzkirch, "Velocity measurements of liquid and gaseous phase for a system of bubbles rising in water," Exp. Fluids **29**, S194–S201 (2000).
[41] R. Lindken and W. Merzkirch, "A novel PIV technique for measurements in multiphase flows and its application to two-phase bubbly flows," Exp. Fluids **33**, 814–825 (2002).
[42] S. Tan, A. Salibindla, A. U. M. Masuk, and R. Ni, "An open-source shake-the-box method and its performance evaluation," in 13th International Symposium on Particle Image Velocimetry, 2019.
[43] R. Ni, S.-D. Huang, and K.-Q. Xia, "Local energy dissipation rate balances local heat flux in the center of turbulent thermal convection," Phys. Rev. Lett. **107**, 174503 (2011).
[44] R. Ni, K.-Q. Xia *et al.*, "Kolmogorov constants for the second-order structure function and the energy spectrum," Phys. Rev. E **87**, 023002 (2013).
[45] T. De Karman and L. Howarth, "On the statistical theory of isotropic turbulence," Proc. R. Soc. London, Ser. A **164**, 192–215 (1938).
[46] R. Ni, N. T. Ouellette, and G. A. Voth, "Alignment of vorticity and rods with Lagrangian fluid stretching in turbulence," J. Fluid Mech. **743**, R3 (2014).